

Organ-specific genome diversity of replication-competent SARS-CoV-2

Jolien Van Cleemput (✉ Jolien.VanCleemput@UGent.be)

Ghent University <https://orcid.org/0000-0003-1598-3057>

Willem van Snippenberg

Ghent University

Laurens Lambrechts

Ghent University

Amélie Dendooven

Ghent University

Valentino D'Onofrio

Jessa Hospital

Liesbeth Couck

Ghent University

Wim Trypsteen

Ghent University <https://orcid.org/0000-0001-9066-4932>

Jan Vanrusselt

Jessa Hospital

Sebastiaan Theuns

PathoSense

Nick Vereecke

Ghent University

Thierry van den Bosch

EC Erasmus

Martin Lammens

University of Antwerp

Ann Driessen

University of Antwerp

Ruth Achten

Jessa Hospital

Ken Bracke

Ghent University <https://orcid.org/0000-0001-5906-4605>

Wim Van Den Broeck

Ghent University

Jan Von der Thüsen

EC Erasmus <https://orcid.org/0000-0001-9699-4860>

Hans Nauwynck

Ghent University

Jo Van Dorpe

Ghent University Hospital

Sarah Gerlo

Ghent University

Piet Maes

Rega Institute for Medical Research <https://orcid.org/0000-0002-4571-5232>

Janneke Cox

Jessa Hospital

Linos Vandekerckhove

HIV Cure Research Center, Ghent University Hospital

Biological Sciences - Article

Keywords: SARS-CoV-2, genome diversity, mutation

Posted Date: April 20th, 2021

DOI: <https://doi.org/10.21203/rs.3.rs-379825/v1>

License:  This work is licensed under a Creative Commons Attribution 4.0 International License.

[Read Full License](#)

Version of Record: A version of this preprint was published at Nature Communications on November 16th, 2021. See the published version at <https://doi.org/10.1038/s41467-021-26884-7>.

Abstract

The coronavirus disease 2019 (COVID-19) pandemic, caused by severe acute respiratory syndrome coronavirus 2 (SARS-CoV-2), has gripped the world for over a year^{1,2}. SARS-CoV-2 impacts people on a broad clinical spectrum from asymptomatic to severe respiratory and systemic manifestations resulting in death³. In addition, intra-host SARS-CoV-2 genomic plasticity periodically leads to emergence of new virus variants with higher transmission capacities⁴⁻⁶. Autopsy series have revealed several pathways to death in COVID-19 patients, including respiratory and multi-organ failure, and evidence of SARS-CoV-2 in various organs besides the lungs^{7,8}. However, these studies did not demonstrate the presence of infectious virus in extrapulmonary sites nor did they investigate viral intra-host evolution across multiple organs. Here we report a detailed virological analysis of thirteen postmortem COVID-19 cases that confirms two stages of fatal disease evolution based on disease duration and viral loads in lungs and plasma⁹. More importantly, the study is the first to provide proof of viremia and presence of replication-competent SARS-CoV-2 in extrapulmonary organs of an immunocompromised patient, accompanied by tissue-specific patterns of genome diversity in organ-resident SARS-CoV-2 populations. In parallel, potentially more transmissible and virulent strains were detected in multiple organs, including identification of mutations N501Y, T1027I, and Y453F in spike (S) protein. These mutations are hallmarks of more contagious United Kingdom (lineage B.1.1.7), South African (lineage B.1.351), Brazilian (lineage P1 and B.1.1.248) or mink variants^{4,10}. Our results provide novel insights about the pathogenesis of SARS-CoV-2 and highlight that COVID-19 treatment and hygiene measures need to be tailored to specific needs of immunocompromised patients.

Main

The lungs and selected extrapulmonary organs (heart, kidney, liver, and spleen) of 13 deceased COVID-19 patients were biopsied postmortem under computed tomography (CT) guidance at the Jessa Hospital, Hasselt, Belgium during the period of April 15th-June 30th 2020. Additionally, plasma was collected from aortic blood and fractionated by ultracentrifugation. Patient demographics and clinical information are summarized in Table S1.

Viral loads in the lungs and RNAemia are higher when patients succumb rapidly to infection

Viral RNA was detected in the lungs and plasma of 9/13 and 8/13 patients, respectively. Cases were then stratified based on duration of disease (short <20 days; long >20 days). Patients who succumbed within 20 days following onset of symptoms generally had a higher viral RNA load in the lungs and plasma when compared to those that had lived longer ($P=0.002$; $F=12.589$; $df=23$; Fig. 1A). Our results support two phases of fatal disease evolution, including (i) short-lived disease with high viral loads in lungs and plasma, associated with a histological pattern of acute exudative alveolar damage in the lungs, and (ii)

long-lived disease with low (or undetectable) viral loads in lungs and plasma, associated with a chronic pattern of lung injury (Fig. 1A and B, Fig. S1). These results agree with findings of another autopsy study⁹. Similarly, intra- and extracellular presence of SARS-CoV-2 nucleocapsid protein (NP) was more frequently identified in the lungs of cases with short-lived disease (4 out of 5), compared to those with long-lived disease (1 out of 8). Over all cases, bronchial epithelial cells and alveolar epithelial cells were the dominant cell type expressing SARS-CoV-2 NP, but we also identified viral NP in alveolar macrophages (Fig. 1B), as described by others^{8,9,11}. Patient 13, who was under rituximab treatment for B cell lymphoma at the time of infection, did not follow the trend and had an exceptionally high viral RNA load in the lungs ($10^{6.5}$ copies/40 ng RNA) and plasma (10^6 copies/mL) after 88 days of disease. SARS-CoV-2 NP was ubiquitously and abundantly found intracellularly and extracellularly in hyaline membranes in the latter patient's lungs, which showed a "remodeling pattern" with interstitial fibrosis and consolidation of airspace (Fig. 1B).

In immunocompromised patients replication-competent SARS-CoV-2 spreads systemically and disseminates to extrapulmonary organs

The frequent detection of SARS-CoV-2 RNAemia (9/13) in this cohort indicates that systemic dissemination of viral components is quite common in severe COVID-19 cases, as described previously¹². However, viremia (i.e., circulation of infectious virions) was found only in one case (patient 13). In this case, VeroE6 cells showed cytopathogenic effects upon inoculation with the plasma pellet, but not after incubation with the other 8 RNAemic plasma pellets (Fig. S2A). Further, intact virions were present in patient 13's plasma pellet, as observed with transmission electron microscopy (Fig. 1C and S2C). These results do not exclude the possibility of viremia in other cases, as current isolation methods might not suffice to isolate virions when viral RNA loads in plasma are below a certain threshold.

Next, we identified two distinct types of disease progression based on viral RNA spread to extrapulmonary organs (i.e. heart, kidney, liver, and/or spleen), with intra-organ spread only occurring in 3 out of 13 cases (Fig. 1D). Digital droplet PCR was run on all biopsies of these three patients to quantify absolute SARS-CoV-2 copy numbers and confirmed spread of viral RNA to multiple organs (Fig. S2B). Viral dissemination to multiple organs was strongly associated with profound immune suppression (chronic high dose corticosteroid and/or rituximab treatment) at the time of infection (Fisher exact $P=0.014$; Table S1). We hypothesize that inadequate immune responses during the early phase of SARS-CoV-2 infection resulted in enhanced viral replication and spread to extrapulmonary organs. Chronic high dose corticosteroid treatment dampens viral-induced danger signals of the host immune response, resulting in impaired release of critical antiviral components (e.g., interferons)^{13,14}. Second, rituximab induces lysis and apoptosis of normal and malignant human B lymphocytes, essential for the production of virus-specific antibodies¹⁵. These findings point out the importance of patient management in severely immunocompromised COVID-19 patients.

Positive SARS-CoV-2 nucleocapsid (NP) staining was found in all organs of case 13, in renal and splenic tissue of case 07 and in splenic tissue of case 06. Viral NP was observed in cardiomyocytes and interstitial cells (heart), podocytes and tubular epithelial cells (kidney), hepatocytes and Kupffer cells (liver) and myeloid cells (spleen) (Fig. 1E). Viral RNA and proteins have been observed multiple times in myeloid cells, tubular cells and podocytes, but this is the first unambiguous evidence of hepatocytes and cardiomyocytes being *in vivo* SARS-CoV-2 targets^{8,16,17}. Interestingly, SARS-CoV-2 NP was detected in cell types expressing both the SARS-CoV-2 main receptor and co-receptor (i.e. angiotensin-converting enzyme type 2 [ACE2] and transmembrane serine protease 2 [TMPRSS2], respectively) across all organs examined (Fig. S3), confirming the *in vivo* relevance of ACE2 and TMPRSS2 in SARS-CoV-2 cell infection.

Further, we isolated virus from extrapulmonary organs that could replicate on VeroE6 cells. Infectious SARS-CoV-2 was isolated from the heart and kidney of case 07 and from all organs of case 13. These progeny viruses were subjected to full-length sequencing to confirm SARS-CoV-2 presence. The fact that we were unable to isolate infectious virus from SARS-CoV-2 RNA- and NP-positive splenic tissue in two out of three cases (case 06 and 07) might indicate that the signal in these tissues derived from phagocytosed virions (and thus, viral RNA and proteins) in immune cells, rather than active viral replication in splenic cells. Viral loads in cardiac tissue of case 06 likely were too low for successful virus isolation. Of note, presence of SARS-CoV-2 in extrapulmonary organs was rarely associated with pathological alterations in the respective organs, except for local cytolysis of cardiomyocytes in the heart. This cytolysis was likely induced by viral replication, and splenic lymphocyte depletion in case 13, which most likely was the result of the rituximab treatment (Fig. 1E, upper right HE images).

SARS-CoV-2 nucleocapsid protein predominates in epithelial cells as well as cells from the myeloid lineage

Although immunohistochemistry analysis can, to a limited extent, identify SARS-CoV-2 target cells, it does not allow marker co-localization at the cellular level. To identify SARS-CoV-2 tissue-specific target cell types in cases with intra-organ viral RNA dissemination (case 06, 07 and 13) we used double immunofluorescence staining and confocal microscopy. As shown in Fig. 2, the majority of SARS-CoV-2 NP-positive cells resided in the lungs (48.73% on a total of 516 positive cells), followed by the kidneys (29.69%), the spleen (10.98%), the liver (9.80%), and the heart (1.68%). SARS-CoV-2 NP was predominantly found in cytokeratin-positive (epithelial) cells in the lungs (67.90%), liver (66.63%), and kidneys (90.90%), while it was more commonly observed in CD14-positive (myeloid) cells in the heart (50.00%) and spleen (57.63%). ICAM-positive (endothelial) cells expressing SARS-CoV-2 NP occasionally were detected in the lungs (7.14%), kidney (3.00%), and spleen (10.02%). In general, SARS-CoV-2 NP was found only in ACE2-positive cells.

Organ-specific SARS-CoV-2 evolution in an immunocompromised patient

We hypothesized that SARS-CoV-2 replication in multiple anatomical compartments would result in the emergence of specific variants in distinct organs, as described for other RNA viruses including poliovirus and HIV^{18,19}. A recent study showed SARS-CoV-2 sequence diversity between respiratory and gastrointestinal tract swabs from three COVID-19 patients²⁰. In general, the SARS-CoV-2 genome changes at a steady mutational rate of 0.0008 substitutions per site per year. As a result, acute respiratory viral infections have low intra-host diversity^{21,22}. However, there is compelling evidence that SARS-CoV-2 evolution is accelerated in the respiratory tract of persistently infected immunocompromised hosts, reflecting reduced selective immune pressure^{6,23–26}. Therefore, we compared viral genome sequences from different organs in a patient with profound systemic and intra-organ viral spread (case 13). The complete clinical history and disease course in case 13 is summarized in Fig. S4.

Phylogenetic analysis confirmed that all SARS-CoV-2 genomes isolated from distinct anatomical compartments of case 13 descended from a common ancestor derived from clade 20B (Fig. 3A). The data show that different populations of viral genomes were found in multiple organs. Consensus viral genomes retrieved from plasma and spleen were phylogenetically most closely related to the founder virus, followed by those from lungs, heart, liver, and kidneys. A more detailed comparative analysis identified 50 (sub-)consensus single nucleotide variations (SNVs) (18 synonymous and 32 non-synonymous mutations), 1 small and 4 large deletions in viral genomes derived from different organs or plasma, as compared to the clade 20B consensus genome (Fig. 3B, Table S2 and S3). These mutations were distributed in the 5' and 3' UTR and across 7 out of 10 protein-coding genes, including *ORF1ab*, *S*, *E*, *ORF7a*, *ORF8*, *N*, and *ORF10*. Three SNVs were fixed in all variants isolated from different compartments (frequencies >94%) and were therefore most likely present in the founder virus. In contrast, all other SNVs and deletions were detected at variable frequencies ranking between 1.11% and 98% depending on tissue origin, illustrating within-host organ-specific evolution of SARS-CoV-2.

Interestingly, several organs harbored viral populations distinct from all other compartments. For instance, four additional SNVs (T7247G, C7279T, and A8387G in *ORF1a*, and A27574T in *ORF7a*) were present at frequencies above 80% in the kidneys (Fig. 3B and Table S2). In addition, six SNVs distributed across *ORF1ab* (A13433G, C16092T, T18024C, T18750C, C18979T) and *ORF10* (C29592T) were almost uniquely retrieved from kidneys. Six out of these ten SNVs were non-synonymous inducing amino acid substitutions in viral proteins including NSP3, NSP14, ORF7a, and ORF10. Still, viral infection capacity was not reduced by the majority of these SNVs (5/6), as these mutations were also identified in the viral progeny of VeroE6 cells inoculated with kidney-derived viruses (Table S2, in bold). NSP3, NSP14 and ORF7a are involved in viral protein processing, viral release, genome replication and immune evasion, while the *in vivo* role of ORF10 is still under debate^{27–30}. Variation in these proteins likely arose during extensive viral replication and spread in the kidneys, as evidenced by the large number of SARS-CoV-2 NP-positive cells in the kidney, and may have favored infection of the kidney following bottleneck events and viral adaptation to local environments. Besides multiple SNVs, the dominant SARS-CoV-2 genotype in renal tissue displayed a 91 bp deletion in ORF8 and a 1927 bp deletion in the N-terminal tail of S protein comprising the receptor-binding domain (RBD) (Fig. S5 and Table S3). The latter deletion in *S*, as well as

a 1947 bp deletion in the same *S* region was found in almost one quarter of the splenic viral population. Further, a 422 bp deletion in *S* a few base pairs upstream of RBD was observed in the majority of liver-derived viral genomes. These deletion mutations did not grow on VeroE6 cells, questioning their *in vivo* infectivity. Still, how these deletion mutants accumulate in multiple organs remains to be elucidated. In this context, similar variants with deletions in *ORF8*, but not *S*, have been detected in patients from different countries and have been associated with milder infection^{31–33}. Interestingly, other coronaviruses have been shown to shift tissue tropism due to deletions in *S* protein³⁴. Alternatively, it is possible that SARS-CoV-2 defective genomes might modulate viral replication or serve as immune decoys, thereby promoting viral persistence, as described for other RNA viruses³⁵. We speculate that *S* deletion mutants may be involved in viral occupation of the kidney, spleen and liver, but not in viral propagation in VeroE6 cells.

Besides the above-described deletions in *S* protein, the viral population in the spleen was characterized by several unique SNVs that did not affect viral infectivity. For instance, we identified mutations in *ORF1ab* (C12513T [T4083M amino acid substitution in NSP8] and C14937T [no amino acid substitution in RNA-dependent RNA polymerase]), *E* (C26351T [A36V amino acid substitution in E protein]) and 3' UTR (G29744A) with frequencies ranging between 33.61 and 64.31% (Table S2). Specific alterations in NSP8 and E protein may favor viral infection or propagation in splenic tissue, as these viral proteins are involved in viral replication and budding³⁶.

Interestingly, in the liver, viral genomes with a 422 bp deletion in *S* consistently displayed the A23063T (N501Y amino acid substitution in *S* protein) alteration, a key mutation found in three important variant strains (South African B.1.351, UK B.1.1.7, and Brazil P1 strain) that promotes viral binding, infectivity and virulence^{4,37,38}. In addition, this mutation is associated with adaptation to rodents³⁷. The same SNV was also present in genomes derived from other organs, but in lower frequencies and independent from the 422 bp deletion. Still, this mutation remained present in viruses propagated in VeroE6 cells from different tissues, highlighting the infection capacity of mutant N501Y viruses.

Similar to the N501Y mutation, we also identified the C24642T (T1027I amino acid substitution) mutation in *S*, present in current strains of the B.1.1.248 lineage, at peaking concentrations of 50% in lungs and plasma, as well as in their viral offspring in VeroE6 cells⁴. In addition, a high SNV variability was detected in viral *S* genes derived from the lungs, which included mutation A22920T at a frequency of 52.52% leading to Y453F amino acid substitution in RBD of *S* protein. Remarkably, this mutation has been suggested to be the hallmark of the “mink variant”. It is believed to increase viral binding to mink ACE2, and presumably also human ACE2¹⁰. However, since genomes with this SNV did not replicate in VeroE6 cells, binding and entry in monkey cells may be reduced. Our results suggest that viral evolution in the respiratory tract, but also in extrapulmonary organs of immunocompromised COVID-19 patients may prompt the emergence of more virulent and contagious SARS-CoV-2 variants with the capacity to infect other species. These results highlight the utmost importance of hygienic and preventive measures to avoid viral spread from and to immune suppressed patients.

Conclusion

Based on our comprehensive virological assessment of postmortem COVID-19 cases, and on previous autopsy series^{7-9,39}, we propose an adapted SARS-CoV-2 pathogenesis model in fatal COVID-19 disease. COVID-19 patients with severe disease initially suffer from extensive SARS-CoV-2 replication in the lungs, often accompanied with RNAemia. These patients may succumb rapidly to infection due to respiratory failure caused by acute exudative viral pneumonia with or without multi-organ failure resulting from the lack of oxygen and/or a detrimental virus-induced cytokine storm. Immunocompetent patients that mount an adequate antiviral response (innate and adaptive) may eventually clear the virus in lungs and plasma and survive the initial phase of disease. However, secondary (extra-)pulmonary manifestations due to SARS-CoV-2 infection (e.g., airspace consolidation, bacterial superinfections, thrombosis, and sepsis) may still result in death later on. In contrast, the impaired antiviral response in immune suppressed individuals paves the way for accelerated viral replication and multi-organ spread with organ-specific evolution. SARS-CoV-2 disseminates through the blood and infects ACE2- and TMPRSS2-expressing cells (e.g., epithelial cells such as tubular cells and hepatocytes) at distinct locations. Here, virus replication is accompanied by further expansion of selected and unselected variants that facilitate colonization of the respective organ. Perhaps such organs may function as a viral reservoir, facilitating virus persistence. Given emergence of specific mutants in distinct anatomical compartments, also found in currently circulating UK (lineage B.1.1.7), South African (lineage B.1.351) and Brazilian (lineage P1) strains, highly transmissible SARS-CoV-2 variants may arise in such patients and potentially spread to other individuals. Patients eventually succumb to pathological alterations caused by extensive viral replication and cellular damage throughout the body, yet mainly in the lungs. These findings highlight the need of tailoring COVID-19 treatment strategies and isolation management to the phase of disease and the patient's immune status.

Methods

Ethics statement

All procedures performed in studies involving human subjects were in accordance with the ethical standards of the institutional and/or national research committee and with the 1964 Helsinki Declaration and its later amendments or comparable ethical standards. Documented approval was obtained from the Ethics Committees of Jessa hospital and Hasselt University (Clinicaltrials.gov identifier: NCT 04366882). Oral consent for sample collection was obtained from the patients' legal representatives. Written consent could not be obtained due to visiting restrictions in the hospital during the pandemic, but written information was provided via registered mail to the patients' legal representative after oral informed consent.

Sample Collection

Minimally invasive autopsy (MIA) was performed on a total of 13 COVID-19 patients at Jessa hospital who succumbed to infection between April 15th and June 30th, 2020. All patients were confirmed for SARS-CoV-2 infection through RT-qPCR analysis performed on nasopharyngeal swabs. Patient demographics and clinical information is summarized in Table S1. MIA was performed within 24 h of death, as described previously⁴⁰. Briefly, tru-cut biopsies were taken under computed tomography (CT)-guidance (14 G biopsy needle, C.R. Bard, Murray Hill, NJ, USA) from lungs, heart, liver, spleen, and kidneys. Tissue samples were either (i) snap-frozen and stored dry at -80°C for cryosectioning and virus isolation, (ii) submerged in RNA-later before snap-freezing and stored at -80°C for RNA and protein analyses, or (iii) fixed in 10% neutral buffered formalin for 72 h prior to embedment in paraffin for hematoxylin-eosin (HE) staining or immunohistochemistry (IHC). Quality of biopsies was confirmed through histological analysis. Blood was collected from the aorta and transferred to citrate or heparin tubes (Vacuette, Greiner Bio-One, Vilvoorde, Belgium). Plasma was collected from these tubes following centrifugation at 2,500 g for 5 min at room temperature and stored at -80°C.

Tissue Homogenization

Tissue homogenates were prepared using bead mill technology by high-speed shaking (50 Hz) of tissues with 5 mm stainless steel beads for 5 min in a TissueLyser LT (Qiagen). Ten % (w/v) solutions of single tissues were made in either (i) RLT buffer (Qiagen, Hilden, Germany) supplemented with 1% β -mercaptoethanol (Sigma-Aldrich, St. Louis, MO, USA) for RNA analyses, (ii) RIPA buffer (Sigma-Aldrich) supplemented with cOmplete™, EDTA-free Protease Inhibitor Cocktail (Roche, Basel, Switzerland) for protein analyses, or (iii) Dulbecco's modified Eagle medium (DMEM; ThermoFisher Scientific, Waltham, MA, USA) supplemented with 8% heat-inactivated fetal bovine serum (FBS; ThermoFisher Scientific), 0.075% sodium bicarbonate (ThermoFisher Scientific) and 1 mM sodium pyruvate (ThermoFisher Scientific) for virus isolation. Finally, tissue homogenates were clarified by centrifugation at 13,000 g for 10 min at 4°C.

Virion Pelleting from Plasma

One mL of plasma (citrate tubes) was diluted in 10 mL of Dulbecco's phosphate-buffered saline (ThermoFisher Scientific) and centrifuged at 45,000 g for 3 h at 4°C using a Sorvall centrifuge (ThermoFisher Scientific) and A27 rotor. Pellets were resuspended in the same three buffers (200 μ L) as described above for tissue samples.

RNA Extraction and cDNA Synthesis

RNA was extracted from clarified tissue homogenates and dissolved plasma pellets using the RNeasy® Plus Mini Kit (Qiagen) following the manufacturer's instructions. Prior to RNA extraction, genomic DNA was removed using a gDNA Eliminator spin column (Qiagen). RNA quantities were measured using

Qubit® RNA BR Assay Kits (ThermoFisher Scientific). A total of 1 µg RNA was reverse-transcribed to cDNA using the SuperScript III First-Strand Synthesis System (ThermoFisher Scientific) following the manufacturer's instructions

qPCR

SARS-CoV-2

Two µL of cDNA was subjected in duplicate to quantitative PCR (qPCR) using a CDC qPCR probe assay (N1, Integrated DNA Technologies, Coralville, IA, USA, Table S4) with LightCycler® 480 Probes Master (Roche). A 10-fold dilution series of 2019-nCoV Plasmid Control (Integrated DNA Technologies), corresponding to a range of 2 to 2×10^5 SARS-CoV-2 RNA copies, functioned as standard. qPCR was performed with a LightCycler® 480 Real-Time PCR System (Roche) with the following amplification conditions: preincubation at 95° for 10 min with 45 cycles of denaturation (30 s at 95°C), annealing (30 s at 55°C), followed by a final elongation for 5 min at 40°C. Sample CT values were plotted against standard dilution values to determine exact SARS-CoV-2 RNA concentrations.

ACE2 and TMPRSS2

Two µL of cDNA was subjected in duplicate to quantitative PCR (qPCR) using LightCycler® 480 SYBR Green I Master (Roche) and specific primers for ACE2⁴¹ and TMPRSS2 (Table S4). Beta-actin (ACTB), glyceraldehyde 3-phosphate dehydrogenase (GAPDH), and YWHA were included as housekeeping genes for normalization of gene expression⁴². No template sample was used as negative control. The qPCR was performed on a LightCycler® 480 Real-Time PCR System (Roche) with the following amplification conditions: preincubation at 95° for 2 min with 45 cycles of denaturation (15 s at 95°C), annealing (30 s at 60°C), and extension (15 s at 72°C), followed by a melting curve from 55°C to 95°C. Relative gene expression was calculated using qbase⁺ software (Biogazelle, Zwijnaarde, Belgium).

ddPCR

Two µL of cDNA was subjected in duplicate to droplet digital PCR (ddPCR) using a CDC qPCR probe assay (N1, Integrated DNA Technologies) with Master mix for probes (Bio-Rad, Hercules, CA, USA). The digital PCR was performed using a QX100™ Droplet Digital™ PCR System (Bio-Rad) with the following amplification conditions: preincubation at 95° for 10 min with 40 cycles of denaturation (30 s at 94°C), annealing (30 s at 56°C), followed by enzyme deactivation for 10 min at 98°C. The ramp rate during the PCR was set at 2°C per second. Samples were read-out using the QX100 Droplet Reader and analyzed with QuantaSoft software (Bio-Rad). Final copy numbers were determined using the ddpcrquant shiny tool with standard settings⁴³.

Whole-Genome Sequencing and Genome Assembly

Whole genome sequencing was performed with Oxford Nanopore Technologies (ONT), shown to accurately detect SNVs and deletions in SARS-CoV-2 genomes²⁵. Following RNA extraction as described above, cDNA was synthesized followed by multiplex PCR amplification using a modified version of the ARTIC V3 LoCost protocol with the Midnight primer set (1,200 bp amplicons)⁴⁴⁻⁴⁶. An additional primer set (A6 with resulting in a 2500 bp amplicon) was used to PCR amplify part of the *S* gene⁴⁵. The libraries were sequenced on a MinION using R9.4.1 flow-cells (Oxford Nanopore Technologies, Oxford, UK). The resulting fast5 reads were basecalled and demultiplexed using Guppy version 4.2.2 in high accuracy mode. Genome assembly was performed using the ARTIC bioinformatics pipeline, which entails adapter trimming, mapping to the reference strain Wuhan-Hu-1 (MN908947) and consensus calling with 20x minimum coverage⁴⁷. The mapping assembly of the viral genome was nearly complete (99.5%) for all samples with a minimum average of 200-fold read depth. SNVs on consensus level were identified via Nanopolish and filtered by the ARTIC *artic_vcf_filter* tool while SNVs at lower frequencies were identified using Varscan2 (v2.4.3)^{48,49}. Additionally, to detect structural variants (SVs) for each sample, an alignment to MN908947 was made via NGMLR (v0.2.7) and subsequently used by Sniffles (v1.0.11) to identify SVs with a minimum size of 10 bp and ≥ 20 supporting reads⁵⁰. Only SNVs with frequencies higher than 20% in at least one anatomical compartment were called.

Phylogenetic Analysis

Public Belgian SARS-CoV-2 genomes with a high coverage were collected on March 12, 2021 from the GISAID database (<https://www.gisaid.org/>) with sampling dates ranging between January 2020 - June 2020. A genome alignment using MAFFT was constructed using the case 13 consensus genomes derived from different anatomical compartments, the Belgian GISAID genomes and the MN908947 reference⁵¹. Clades for each sequence were assigned via Nextclade⁵². Using the nextstrain toolkit, a maximum-likelihood phylogenetic tree was constructed via IQ-Tree V1.6.9, using a GTR substitution model and performing 100 bootstraps with annotation and visualization done via iTol⁵³⁻⁵⁵.

ELISA

Protein levels in clarified tissue homogenates and pure plasma (heparin) were determined using the Pierce™ Detergent Compatible Bradford Assay Kit (ThermoFisher Scientific) according to the manufacturer's instructions. ACE2 and TMPRSS2 levels were quantified using the human ACE2 ELISA Kit (ab235649; Abcam, Cambridge, United Kingdom) and human TMPRSS2 ELISA Kit (NBP2-89171; Novus Biologicals, Centennial, CO, USA), respectively, according to the manufacturers' instructions. Finally, protein concentrations were normalized to total protein content (ng/mg total protein).

Immunohistochemistry

Four μm -thick formalin-fixed and paraffin-embedded sections were cut and subjected to immunohistochemistry. SARS-CoV-2 nucleocapsid protein (NP) was stained by automated IHC using the Discovery ULTRA platform (Ventana Medical Systems, Oro Valley, AZ, USA). Sections were deparaffinized prior to heat-induced antigen retrieval with CC1 (#950-500, Ventana Medical Systems) for 32 min. Next, slides were incubated with a rabbit polyclonal anti-SARS-CoV-2 nucleocapsid protein (NP) antibody (40143-T62; Sinobiological, Beijing, China) for 32 minutes at 37°C. Detection was done with omnimap-anti-Rabbit HRP (#760-4311, Ventana Medical Systems) for 16 minutes and visualized with Discovery Purple (#760-229, Ventana Medical Systems) for 32 minutes. Incubation was followed by hematoxylin II counter stain for 4 minutes and then a blue coloring reagent for 4 minutes according to the manufacturers' instructions (Ventana Medical Systems). ACE2 was immune-stained using polyclonal rabbit anti-human ACE2 antibodies (#ab15348; Abcam), as described previously⁵⁶. TMPRSS2 was stained using monoclonal rabbit anti-human TMPRSS2 (#ab109131; Abcam) following heat-mediated antigen retrieval in Tris/EDTA buffer pH 9. In the second step, horseradish peroxidase (HRP)-labelled poly anti-rabbit IgG antibodies (#DPVR-55HPR; Immunologic, Duiven, The Netherlands) were added. Immunostaining was visualized using DAB+ (Agilent, Santa Clara, CA, USA) and hematoxylin II was used for counterstaining. Positive controls were used on every slide. Rabbit monoclonal or polyclonal isotype antibodies functioned as negative controls (#ab172730 and #ab15348; Abcam).

Immunofluorescence Staining and Confocal Microscopy Analysis

Ten μm thick cryosections were double stained using a monoclonal mouse anti-SARS-CoV-2 antibody (#MBS569903; MyBioSource, San Diego, CA, USA) and one of the following antibodies: polyclonal rabbit anti-pan cytokeratin antibody (#ab9377; Abcam), monoclonal rabbit anti-CD14 antibody (#ab18332; Abcam), polyclonal rabbit anti-ACE2 (#PK-AB718-3217, PromoCell, Heidelberg, Germany), monoclonal rabbit anti-ICAM-1 (#ab109361, Abcam). Mouse monoclonal and rabbit monoclonal or polyclonal isotype antibodies (#ab18469, #ab172730 and #ab15348; Abcam) functioned as negative controls. In the secondary step, FITC-conjugated polyclonal goat anti-mouse antibodies were combined with Texas Red-conjugated polyclonal donkey anti-rabbit antibodies (ThermoFisher Scientific). In the tertiary step, FITC-conjugated polyclonal donkey anti-goat antibodies were added (ThermoFisher Scientific). DAPI was used to counterstain cell nuclei. Slides were mounted with Fluoroshield™ (Sigma-Aldrich) and analyzed using a Leica (TCS SPE) confocal microscope.

Transmission Electron Microscopy

Seven μL of pelleted plasma resuspended in complete medium was spotted onto copper hexagonal EM grids (Electron Microscopy Sciences, Hatfield, PA, USA). Complete medium only or plasma of a COVID-19-

negative patient and a virus stock of porcine respiratory coronavirus (strain 20v17) functioned as negative and positive controls, respectively (Fig. S2C). Grids were washed one time in ultrapure water prior to negative staining with 1% uranyl acetate for 45 seconds. EM grids were observed using a JEOL JEM-1400 Plus transmission electron microscope.

Virus Isolation

Tissue homogenates and resuspended plasma pellets were added to 90% confluent Vero E6 cell (ATCC C1008) monolayers (6-well format) and incubated on a plate rocker for 2 h at 35° C. After 2 washes with an excess of sterile PBS, fresh Dulbecco's Modified Eagle's medium (ThermoFisher Scientific) supplemented with 2% heat-inactivated FBS (Sigma-Aldrich) and 2 mg/ml trypsin (ThermoFisher Scientific) was added and plates were incubated in a humidified 5% CO₂ atmosphere at 37 °C. Cells were daily monitored for cytopathogenic effect (CPE) for a maximum of 21 days. The cell medium was replaced every 7 days.

Statistical Analysis

Significant differences were identified by a Student's t-test (2 groups) or analysis of variance (ANOVA) followed by a Tukey post-hoc test (multiple groups). If homoscedasticity of the variables was not met, as assessed by Levene's test, the data were log-transformed prior to t-tests or ANOVA. The normality of the residuals was verified using the Shapiro-Wilk test. If the variables remained heteroscedastic or normality was not met after log transformation, a Mann-Whitney's test (2 groups) or Kruskal-Wallis test (multiple groups) was performed. Significance of the associations were determined using the Fisher's exact test. All analyses were conducted in IBM SPSS Statistics, version 27.0 (IBM Corp., Armonk, NY, USA).

Declarations

Acknowledgements

The authors acknowledge Ann Neesen, Indra De Borle and Carine Boone for their excellent technical support. We thank Prof. dr. Lynn Enquist for his critical comments on the project and English language editing.

Funding

This research was supported by FWO COVID-19 grants G0G2620N (J.C., A.De., J.V., M.L., A. Dr.) and G0G4520N (L.V.D.K. and S.G.). J.V.C. is a post-doctoral researcher funded by the Research Foundation Flanders (FWO grant 12ZB921N). L.L. was supported by the Research Foundation Flanders (FWO grant 1S29220N). T.V.D.B. and J.V.D.T received funding of ZonMW (grant 10430012010016).

Author contributions

J.V.C designed and coordinated the study, performed and analyzed experiments and wrote the manuscript. W.V.S. helped to perform and analyze experiments. L.L., N.V., S.T. and P.M. performed and analyzed whole genome sequencing. V.D.O., J.V. and J.C. coordinated and performed minimal invasive autopsies. W.T. helped to analyze PCR results and A.De., M.L., A.Dr., R.A. and J.V.D. performed the pathological analysis. Electron microscopy investigation was performed by L.C. in the lab of W.V.D.B., and immunohistochemistry analysis was done by the lab of K.B. (ACE2 and TMPRSS2) and by T.V.D.B. in the lab of J.V.D.T (SARS-CoV-2 NP). The lab of H.N. assisted in immunofluorescence staining and provided the confocal microscope. P.M. performed virus isolations. S.G., J.C., and L.V.D.K. supervised the study. All authors discussed the results, reviewed the manuscript and approved the final version.

Competing Interests

The authors declare no competing interests.

References

1. da Silva, P. G., Mesquita, J. R., de São José Nascimento, M. & Ferreira, V. A. M. Viral, host and environmental factors that favor anthroozoonotic spillover of coronaviruses: An opinionated review, focusing on SARS-CoV, MERS-CoV and SARS-CoV-2. *Sci. Total Environ.***750**, 141483 (2021).
2. Phan, T. Genetic diversity and evolution of SARS-CoV-2. *Infect. Genet. Evol.***81**, 104260 (2020).
3. Robba, C., Battaglini, D., Pelosi, P. & Rocco, P. R. M. Multiple organ dysfunction in SARS-CoV-2: MODS-CoV-2. *Expert Rev. Respir. Med.***14**, 865–868 (2020).
4. Toovey, O. T. R., Harvey, K. N., Bird, P. W. & Tang, J. W.-T. W.-T. Introduction of Brazilian SARS-CoV-2 484K.V2 related variants into the UK. *J. Infect.* S0163-4453(21)00047–5 (2021) doi:10.1016/j.jinf.2021.01.025.
5. Tang, J. W., Tambyah, P. A. & Hui, D. S. Emergence of a new SARS-CoV-2 variant in the UK. *J. Infect.* S0163-4453(20)30786–6 (2020) doi:10.1016/j.jinf.2020.12.024.
6. Karamitros, T. *et al.* SARS-CoV-2 exhibits intra-host genomic plasticity and low-frequency polymorphic quasispecies. *J. Clin. Virol. Off. Publ. Pan Am. Soc. Clin. Virol.***131**, 104585–104585 (2020).
7. Vincent, J.-L. & Taccone, F. S. Understanding pathways to death in patients with COVID-19. *Lancet Respir. Med.***8**, 430–432 (2020).
8. Trypsteen, W., Van Cleemput, J., Snippenberg, W. van, Gerlo, S. & Vandekerckhove, L. On the whereabouts of SARS-CoV-2 in the human body: A systematic review. *PLOS Pathog.***16**, e1009037 (2020).

9. Desai, N. *et al.* Temporal and spatial heterogeneity of host response to SARS-CoV-2 pulmonary infection. *Nat. Commun.***11**, 6319 (2020).
10. Welkers, M. R. A., Han, A. X., Reusken, C. B. E. M. & Eggink, D. Possible host-adaptation of SARS-CoV-2 due to improved ACE2 receptor binding in mink. *Virus Evol.***7**, (2021).
11. Wölfel, R. *et al.* Virological assessment of hospitalized patients with COVID-2019. *Nature***581**, 465–469 (2020).
12. Hogan, C. A. *et al.* High Frequency of SARS-CoV-2 RNAemia and Association With Severe Disease. *Clin. Infect. Dis. Off. Publ. Infect. Dis. Soc. Am.* ciaa1054 (2020) doi:10.1093/cid/ciaa1054.
13. Cain, D. W. & Cidlowski, J. A. Immune regulation by glucocorticoids. *Nat. Rev. Immunol.***17**, 233–247 (2017).
14. Matthay, M. A. & Wick, K. D. Corticosteroids, COVID-19 pneumonia, and acute respiratory distress syndrome. *J. Clin. Invest.***130**, 6218–6221 (2020).
15. Cerny, T., Borisch, B., Introna, M., Johnson, P. & Rose, A. L. Mechanism of action of rituximab. *Anticancer. Drugs***13**, (2002).
16. Wang, Y. *et al.* SARS-CoV-2 infection of the liver directly contributes to hepatic impairment in patients with COVID-19. *J. Hepatol.***73**, 807–816 (2020).
17. Tavazzi, G. *et al.* Myocardial localization of coronavirus in COVID-19 cardiogenic shock. *Eur. J. Heart Fail.***22**, 911–915 (2020).
18. Xiao, Y. *et al.* Poliovirus intrahost evolution is required to overcome tissue-specific innate immune responses. *Nat. Commun.***8**, 375 (2017).
19. Rozera, G. *et al.* Quasispecies tropism and compartmentalization in gut and peripheral blood during early and chronic phases of HIV-1 infection: possible correlation with immune activation markers. *Clin. Microbiol. Infect.***20**, 0157–0166 (2014).
20. Wang, Y. *et al.* Intra-host variation and evolutionary dynamics of SARS-CoV-2 populations in COVID-19 patients. *Genome Med.***13**, 30 (2021).
21. Lythgoe, K. A. *et al.* SARS-CoV-2 within-host diversity and transmission. *Science* eabg0821 (2021) doi:10.1126/science.abg0821.
22. Rambaut, A. Phylodynamic Analysis of SARS-CoV-2 genomes. *Arctic Network* <https://virological.org/t/phylodynamic-analysis-176-genomes-6-mar-2020/356> (2021).
23. Choi, B. *et al.* Persistence and Evolution of SARS-CoV-2 in an Immunocompromised Host. *N. Engl. J. Med.***383**, 2291–2293 (2020).
24. McCarthy, K. R. *et al.* Recurrent deletions in the SARS-CoV-2 spike glycoprotein drive antibody escape. *Science* eabf6950 (2021) doi:10.1126/science.abf6950.
25. Bull, R. A. *et al.* Analytical validity of nanopore sequencing for rapid SARS-CoV-2 genome analysis. *Nat. Commun.***11**, 6272–6272 (2020).
26. Kemp, S. A. *et al.* SARS-CoV-2 evolution during treatment of chronic infection. *Nature* (2021) doi:10.1038/s41586-021-03291-y.

27. Shin, D. *et al.* Papain-like protease regulates SARS-CoV-2 viral spread and innate immunity. *Nature***587**, 657–662 (2020).
28. Taylor, J. K. *et al.* Severe Acute Respiratory Syndrome Coronavirus ORF7a Inhibits Bone Marrow Stromal Antigen 2 Virion Tethering through a Novel Mechanism of Glycosylation Interference. *J. Virol.***89**, 11820 (2015).
29. Pancer, K. *et al.* The SARS-CoV-2 ORF10 is not essential in vitro or in vivo in humans. *PLOS Pathog.***16**, e1008959 (2020).
30. Ogando, N. S. *et al.* The Enzymatic Activity of the nsp14 Exoribonuclease Is Critical for Replication of MERS-CoV and SARS-CoV-2. *J. Virol.***94**, e01246-20 (2020).
31. Young, B. E. *et al.* Effects of a major deletion in the SARS-CoV-2 genome on the severity of infection and the inflammatory response: an observational cohort study. *The Lancet***396**, 603–611 (2020).
32. Su, Y. C. F. *et al.* Discovery and Genomic Characterization of a 382-Nucleotide Deletion in ORF7b and ORF8 during the Early Evolution of SARS-CoV-2. *mBio***11**, e01610-20 (2020).
33. Gong, Y.-N. *et al.* SARS-CoV-2 genomic surveillance in Taiwan revealed novel ORF8-deletion mutant and clade possibly associated with infections in Middle East. *Emerg. Microbes Infect.***9**, 1457–1466 (2020).
34. Saif, L. J., Wang, Q., Vlasova, A. N., Jung, K. & Xiao, S. Coronaviruses. in *Diseases of Swine* 488–523 (John Wiley & Sons, Ltd, 2019). doi:10.1002/9781119350927.ch31.
35. Rezelj, V. V., Levi, L. I. & Vignuzzi, M. The defective component of viral populations. *Virus Vector Interact. • Spec. Sect. Multicomponent Viral Syst.***33**, 74–80 (2018).
36. Amor, S., Fernández Blanco, L. & Baker, D. Innate immunity during SARS-CoV-2: evasion strategies and activation trigger hypoxia and vascular damage. *Clin. Exp. Immunol.***202**, 193–209 (2020).
37. Gu, H. *et al.* Adaptation of SARS-CoV-2 in BALB/c mice for testing vaccine efficacy. *Science***369**, 1603 (2020).
38. Starr, T. N. *et al.* Deep Mutational Scanning of SARS-CoV-2 Receptor Binding Domain Reveals Constraints on Folding and ACE2 Binding. *Cell***182**, 1295-1310.e20 (2020).
39. Damiani, S. *et al.* Pathological post-mortem findings in lungs infected with SARS-CoV-2. *J. Pathol.***253**, 31–40 (2021).
40. D’Onofrio, V. *et al.* The clinical value of minimal invasive autopsy in COVID-19 patients. *PLOS ONE***15**, e0242300 (2020).
41. Song, J. *et al.* Distinct effects of asthma and COPD comorbidity on disease expression and outcome in patients with COVID-19. *Allergyn/a*, (2020).
42. Janssens, J. *et al.* Evaluating the applicability of mouse SINES as an alternative normalization approach for RT-qPCR in brain tissue of the APP23 model for Alzheimer’s disease. *J. Neurosci. Methods***320**, 128–137 (2019).
43. Trypsteen, W. *et al.* ddpcRquant: threshold determination for single channel droplet digital PCR experiments. *Anal. Bioanal. Chem.***407**, 5827–5834 (2015).

44. Freed, N. E., Vlková, M., Faisal, M. B. & Silander, O. K. Rapid and inexpensive whole-genome sequencing of SARS-CoV-2 using 1200 bp tiled amplicons and Oxford Nanopore Rapid Barcoding. *Biol. Methods Protoc.***5**, (2020).
45. Eden, J.-S. *et al.* An emergent clade of SARS-CoV-2 linked to returned travellers from Iran. *Virus Evol.***6**, (2020).
46. Tyson, J. R. *et al.* Improvements to the ARTIC multiplex PCR method for SARS-CoV-2 genome sequencing using nanopore. *bioRxiv* 2020.09.04.283077 (2020) doi:10.1101/2020.09.04.283077.
47. Loman, N., Rowe, W. & Rambaut, A. nCoV-2019 novel coronavirus bioinformatics protocol. *Arctic Network* <https://artic.network/ncov-2019/ncov2019-bioinformatics-sop.html> (2020).
48. Simpson, J. T. *et al.* Detecting DNA cytosine methylation using nanopore sequencing. *Nat. Methods***14**, 407–410 (2017).
49. Koboldt, D. C. *et al.* VarScan 2: Somatic mutation and copy number alteration discovery in cancer by exome sequencing. *Genome Res.***22**, 568–576 (2012).
50. Sedlazeck, F. J. *et al.* Accurate detection of complex structural variations using single-molecule sequencing. *Nat. Methods***15**, 461–468 (2018).
51. Katoh, K. & Standley, D. M. MAFFT Multiple Sequence Alignment Software Version 7: Improvements in Performance and Usability. *Mol. Biol. Evol.***30**, 772–780 (2013).
52. Aksamentov, I. & Neher, R. Nextstrain/nextclade. *GitHub* <https://github.com/nextstrain/nextclade> (2020).
53. Nguyen, L.-T., Schmidt, H. A., von Haeseler, A. & Minh, B. Q. IQ-TREE: A Fast and Effective Stochastic Algorithm for Estimating Maximum-Likelihood Phylogenies. *Mol. Biol. Evol.***32**, 268–274 (2015).
54. Letunic, I. & Bork, P. Interactive tree of life (iTOL) v3: an online tool for the display and annotation of phylogenetic and other trees. *Nucleic Acids Res.***44**, W242–W245 (2016).
55. Hadfield, J. *et al.* Nextstrain/ncov. *GitHub* <https://github.com/nextstrain/ncov> (2020).
56. Wijnant, S. R. A. *et al.* Expression of ACE2, the SARS-CoV-2 Receptor, in Lung Tissue of Patients With Type 2 Diabetes. *Diabetes***69**, 2691 (2020).

Figures

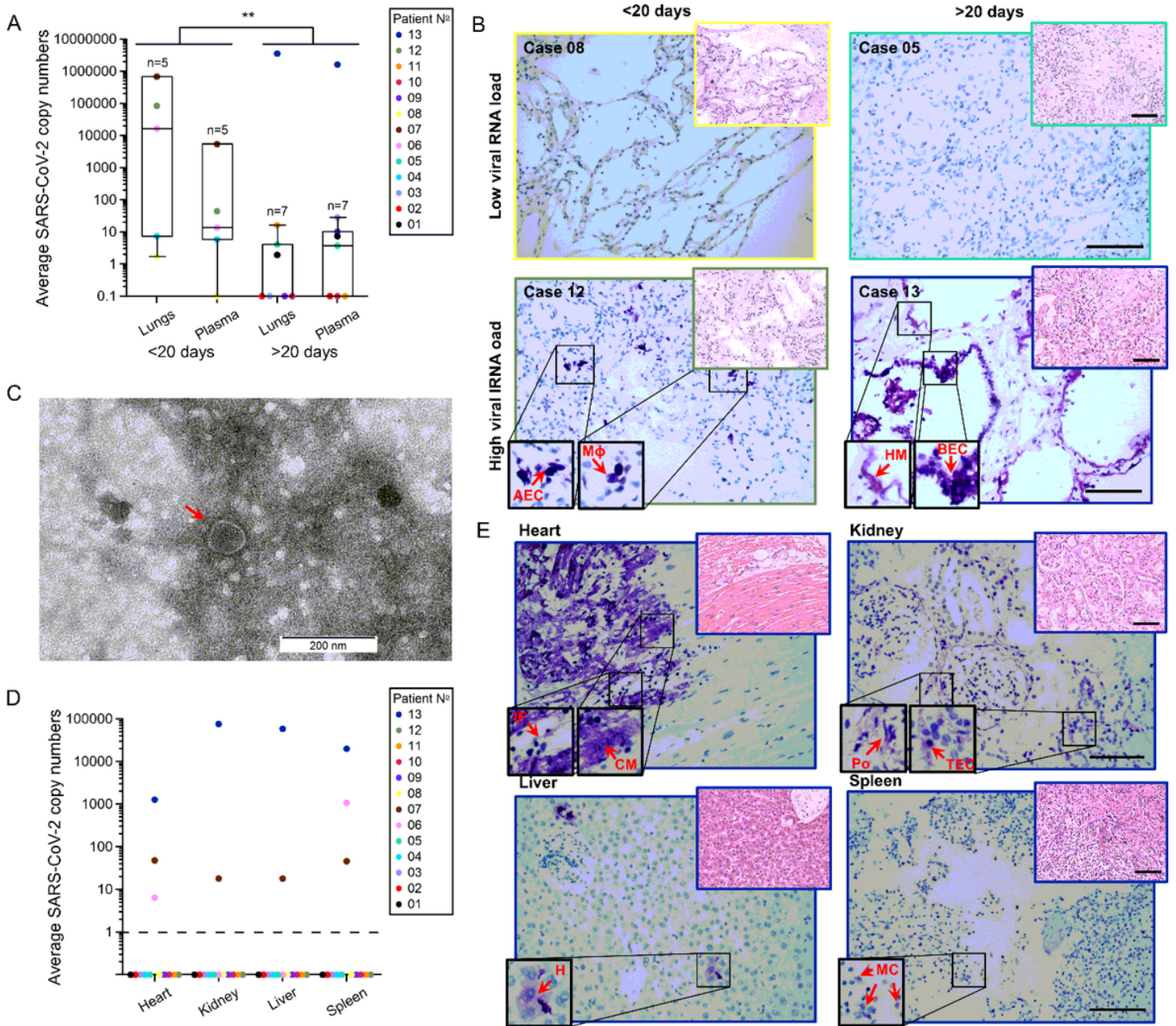


Figure 1

Detailed virological analysis of 13 postmortem COVID-19 cases. (A) SARS-CoV-2 RNA loads on a total of 40 ng RNA, as measured with RT-qPCR, in the lungs of different cases (different colors) with short- or long-lived disease (<20 or >20 days after onset of symptoms, respectively). Significant differences are indicated by asterisks: **, $P < 0.01$. (B) SARS-CoV-2 nucleocapsid (NP) staining (in purple; large images and 2X-enlarged smaller images in the lower left corners) and hematoxylin (HE) staining (small images in upper right corners) of paraffin-embedded sections of lung tissue of four different cases with low (<5 copies/40ng RNA) or high (>5 copies/40ng RNA) viral RNA loads and short- or long-lived disease. Arrows show specific SARS-CoV-2 NP-positive cells or hyaline membranes (HM). All scale bars represent 100 μm . Abbreviations: AEC= alveolar epithelial cell, BEC= bronchial epithelial cell, EC= endothelial cell, M ϕ = macrophage. (C) Transmission electron microscopic image of a SARS-CoV-2 particle (indicated by the

arrow) derived from plasma of case 13. Positive and negative controls are shown in Fig. S2C. Scale bar indicates 200 nm. (D) SARS-CoV-2 RNA loads on a total of 40 ng RNA, as measured with RT-qPCR, in selected extrapulmonary organs. (E) SARS-CoV-2 NP staining on paraffin-embedded sections of extrapulmonary tissues of case 13. Arrowheads indicate SARS-CoV-2 NP-positive cells. Abbreviations: CM= cardiomyocyte, IF=interstitial fibroblast, H= hepatocyte, MC= myeloid cell, Po= podocyte, TEC= tubular epithelial cell. All scale bars represent 100 µm.

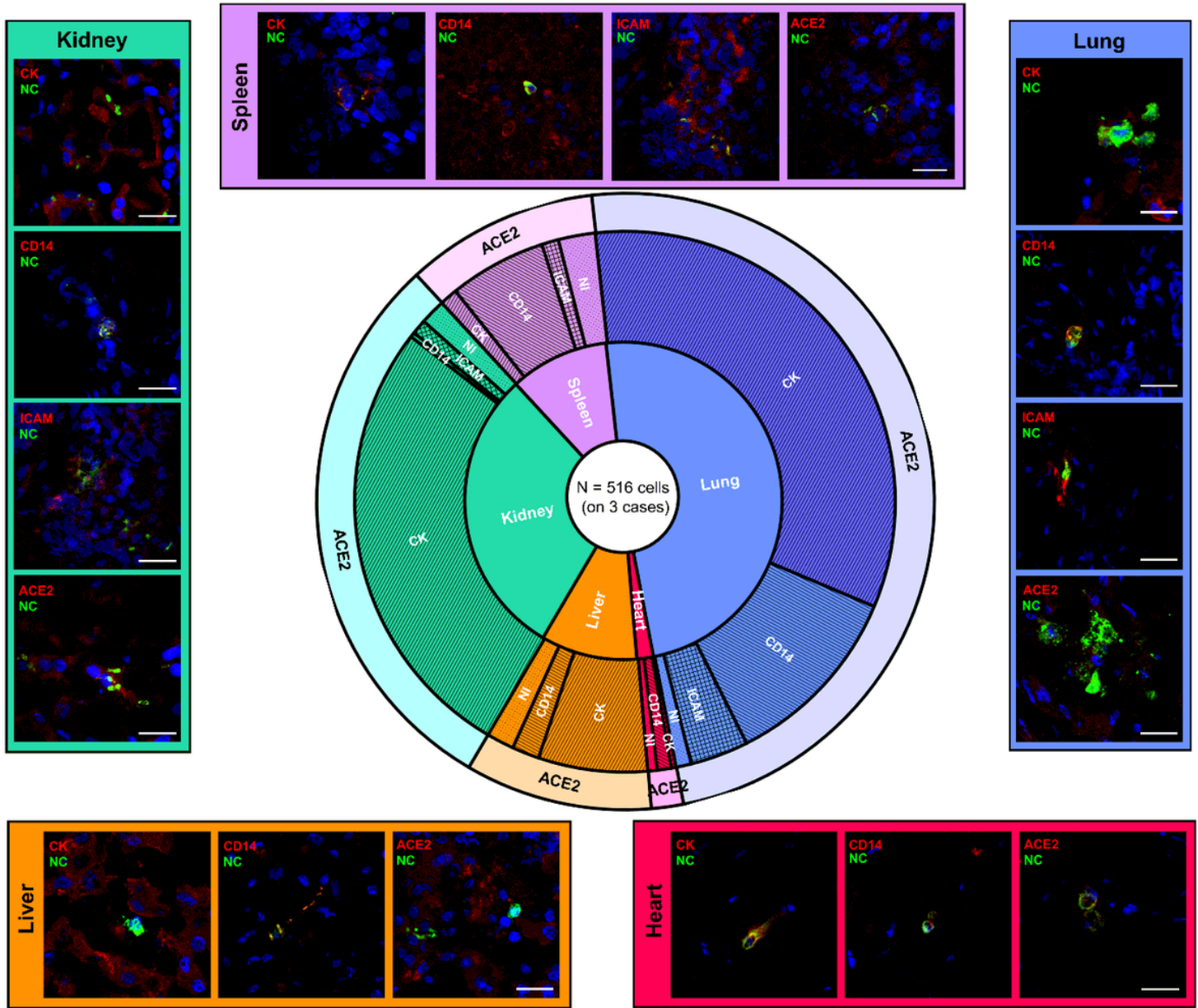


Figure 2

Delineation of SARS-CoV-2 NP-positive cells and total viral burden from postmortem biopsies, by tissue type. A total of 516 SARS-CoV-2 nucleocapsid protein (NP)-positive cells were evaluated for marker expression (123 for ACE2, 133 for cytokeratin [CK], 136 for CD14, and 120 for ICAM) across different organs of three cases with viral dissemination (case 06, 07 and 13). The first level of the sunburst chart represents the distribution of SARS-CoV-2 NP-positive cells across different organs (blue= lung, red= heart, brown= liver, green= kidney, purple= spleen). The second level of the sunburst chart depicts the

percentage of cell types positive for SARS-CoV-2 NP per organ (forward slash= cytokeratin [CK], backward slash= CD14, crosshatch= ICAM, dotted= not identified [NI]), and the third level shows co-localization data with ACE2. Representative confocal images are grouped per organ (different colors) at the outer edges. Scale bars represent 25 μ m.

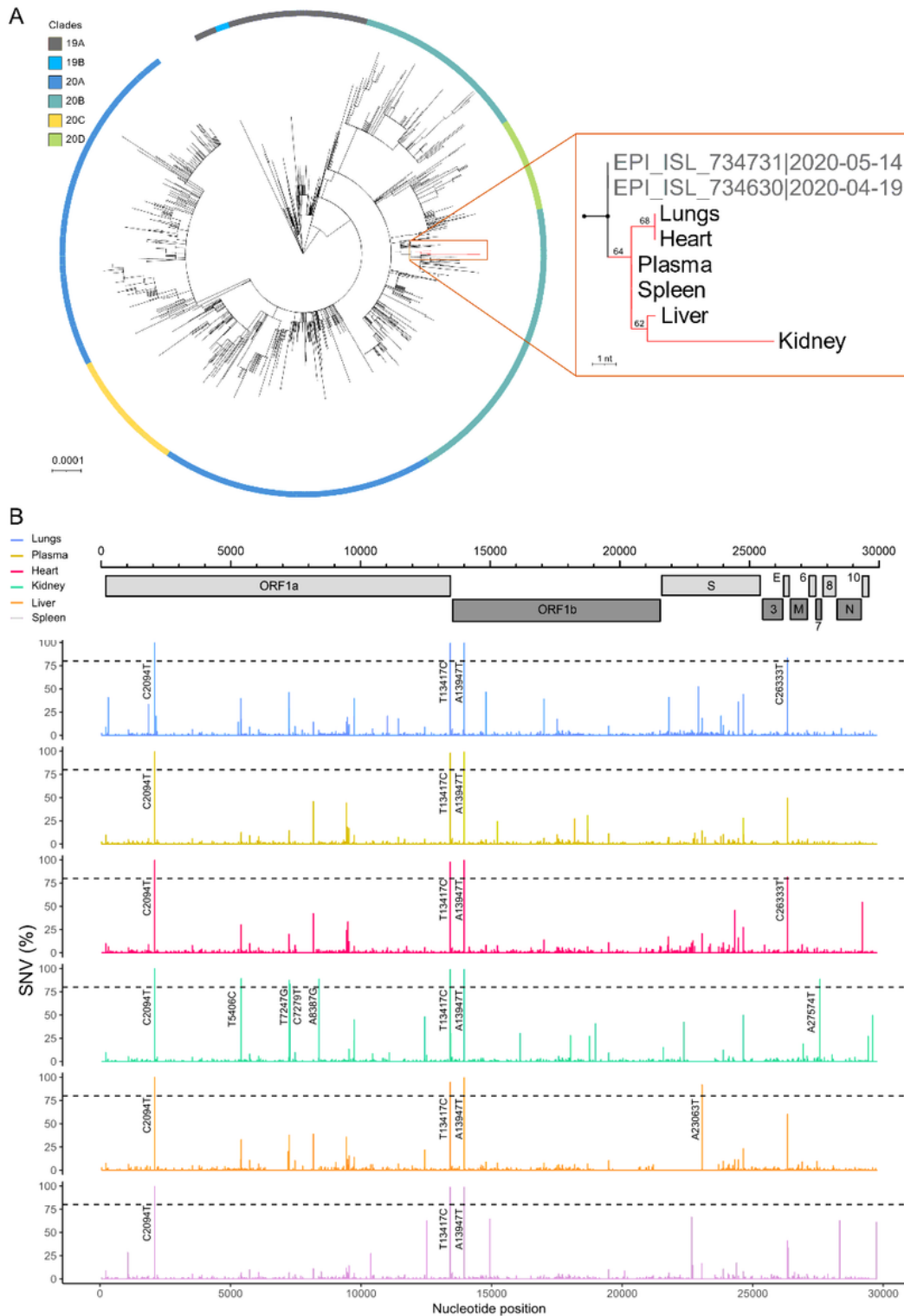


Figure 3

Tissue-specific SARS-CoV-2 evolution in an immune suppressed individual with profound viral spread. (A) Left: A circular maximum-likelihood phylogenetic tree rooted against the Wuhan-Hu-1 reference sequence, including SARS-CoV-2 consensus genomes from case 13 (in red) and public Belgian genomes from GISAID sampled between January 2020 and June 2020. The scale is proportional to the number of substitutions per site. Right: A detailed sub-tree highlighting case 13, displaying the underlying relation between the different anatomical compartments. Bootstrap values above 50 are shown. GISAID references are given in Table S5. (B) SARS-CoV-2 genome variations as compared to clade 20B consensus genome listed per anatomical compartment (different colors). Nucleotide positions and single nucleotide variation (SNV) frequencies are indicated on the X axis and the Y axis, respectively. SNVs with frequencies above 80% are annotated. A complete list of SNVs with allele frequencies per anatomical compartment can be found in Table S2.

Supplementary Files

This is a list of supplementary files associated with this preprint. Click to download.

- [Supplementaryinformation.docx](#)